Evaluation of the mechanical performance of a composite multi-cell tank for cryogenic storage

Part II – Experimental assessment

Tapeinos, Ilias G.; Rajabzadeh, Aydin; Zarouchas, Dimitrios S.; Stief, Malte; Groves, Roger M.; Koussios, Sotiris; Benedictus, Rinze

DOI
10.1016/j.ijhydene.2018.12.063

Publication date
2019

Document Version
Final published version

Published in
International Journal of Hydrogen Energy

INTERNATIONAL JOURNAL OF HYDROGEN ENERGY 44 (2019) 3931–3943

Available online at www.sciencedirect.com

ScienceDirect

journal homepage: www.elsevier.com/locate/he

Evaluation of the mechanical performance of a composite multi-cell tank for cryogenic storage: Part II – Experimental assessment

Ilias G. Tapeinos [a,*], *Aydin Rajabzadeh* [a], *Dimitrios S. Zarouchas* [a], *Malte Stief* [b], *Roger M. Groves* [a], *Sotiris Koussios* [a], *Rinze Benedictus* [a]

[a] *Structural Integrity & Composites Group, Faculty of Aerospace Engineering, Delft University of Technology, Kluyverweg 1, HS Delft, 2629 Netherlands*

[b] *Institute of Space Systems, German Aerospace Center, Robert-Hooke-Straße 7, 28359 Bremen, Germany*

ARTICLE INFO

Article history:
Received 1 August 2018
Received in revised form
27 November 2018
Accepted 7 December 2018
Available online 31 December 2018

Keywords:
Multi-cell tank
Hydrostatic burst
Cryo-cycling
Strain monitoring
Damage progression

ABSTRACT

This study focuses on the understanding of the thermal and structural behavior of an innovative Type IV multi-spherical composite-overwrapped pressure vessel through an experimental assessment that consists of hydrostatic testing at ambient conditions and pressure cycling with a cryogenic medium (LN_2). During hydro-burst testing at a high displacement rate, the strain and damage progression is monitored with Digital-Image-Correlation (DIC) and Acoustic Emission (AE) techniques respectively. The effect of filling with LN_2, pressure cycling and draining on the composite overwrap temperature gradient and strain evolution is additionally obtained with Fiber Bragg Gratings (FBGs) and thermocouples. Utilization of AE helped to reveal the different damage mechanisms occurring and enabled the evaluation of the pressure window of the multi-sphere. The experimental measurements in the cryogenic regime verified the suitability of the involved stiffness and coefficient of thermal expansion (CTE) fitting functions developed in [32] that enable to establish of a relationship between strain and temperature during cryogenic chill-down and pressure cycling. This study provides a framework about the suitability of conformal Type IV multi-spherical COPVs for cryogenic storage.

Introduction

Hydrogen (H_2) is considered as an environmentally friendly solution compared to the conventional hydrocarbon fuels used in today's aircraft engines as well as a strong candidate for future aviation fuel, associated to is high gravimetric energy density [1,2]. However, the volumetric energy density of H_2 is only a quarter of the corresponding value of kerosene at ambient conditions and can only be increased by compression or liquefaction. Liquid hydrogen (LH_2) has a volumetric energy density that is twice as high as the gaseous hydrogen (GH_2) pressurized at 700 [bar] [3]. Therefore, LH_2 tanks are expected to have high volumetric efficiency within a pre-defined allowable mounting space in the aircraft.

DOI of original article: https://doi.org/10.1016/j.ijhydene.2018.12.118.
* Corresponding author.
E-mail address: I.Tapeinos@tudelft.nl (I.G. Tapeinos).
URL: http://www.tudelft.nl/
https://doi.org/10.1016/j.ijhydene.2018.12.063
0360-3199/

Nomenclature

Abbreviations

AE	Acoustic Emission
AIAA	American Institute of Aeronautics and Astronautics
ANSI	American National Standards Institute
CFRP	Carbon Fiber Reinforced Polymer
CLT	Classical Lamination Theory
COPV	Composite Overwrapped Pressure Vessel
CTE	Coefficient of Thermal Expansion
DIC	Digital Image Correlation
DTG	Draw Tower Grating
FBGs	Fiber Bragg Gratings
FPF	First Ply Failure
FE	Finite Element
GH_2	Gaseous Hydrogen
GN2	Gaseous Nitrogen
IPC	Industrial Personal Computer
LH_2	Liquid Hydrogen
LN_2	Liquid Nitrogen
LPF	Last Ply Failure
MECO	Main Engine Cut-off
MEOP	Maximum Expected Operating Pressure
PA	Polyamide
PFA	Progressive Failure Analysis
QI	Quasi-Isotropic
RLV	Re-usable Lightweight Vehicle
UD	Uni-directional

Symbols

a, b, c, α_o	Coefficients of the least-squares approximation, [-]
$a_{[0^\circ]}$	Number of UD straps at [0°] orientation, [-]
$a_{[\pm 45^\circ]}$	Number of UD straps at [±45] orientation, [-]
$\mathbf{A}_{\text{sphere}}$	$_{\text{sphere}}$Extensional matrix of the laminate at the sphere, [N/mm]
$\mathbf{A}_{\text{sphere}}(T)$	Extensional matrix of the laminate at the sphere as a function of temperature,[N/mm]
$\mathbf{A}_{\text{torus}}$	Extensional matrix of the laminate at the intersection, [N/mm]
$\mathbf{A}_{\text{torus}}(T)$	Extensional matrix of the laminate at the intersection as a function of temperature, [N/mm]
$\mathbf{C}_{[\varphi]_k}(T)$	Reduced stiffness ply matrix of k layer as a function of temperature, [MPa]
d	Sphere centroids distance, [mm]
dP	Pressure difference between P_{FPF} and P_{LPF} of the multi-sphere, [bar]
dP_fast_FE	Pressure difference between P_{FPF} and P_{LPF} of the multi-sphere when loaded at a high pressure rise rate (from FE analysis), [bar]
dP_fast_exp	Pressure difference between P_{FPF} and P_{LPF} of the multi-sphere when loaded at a high pressure rise rate (from experiment), [bar]
dP_slow_FE	Pressure difference between P_{FPF} and P_{LPF} of the multi-sphere when loaded at a low pressure rise rate (from FE analysis), [bar]
dP/dt	Pressure rise rate, [bar]
$\mathbf{D}_{\text{sphere}}$	$_{\text{sphere}}$Bending stiffness matrix of the laminate at the sphere, [Nmm]
$\mathbf{D}_{\text{torus}}$	$_{\text{torus}}$Bending stiffness matrix of the laminate at the intersection, [Nmm]
$\mathbf{D}_{\text{torus}}(T)$	Bending stiffness matrix of the laminate at the intersection, as a function of temperature,[Nmm]
$\mathbf{e}_{\text{free}}^{[0^\circ]}, \mathbf{e}_{\text{free}}^{[90^\circ]}$	Free expansion strain vector for [0°] and [90°] ply, [-]
$E_{11}^T, E_{22}^T, G_{12}^T$	Ply engineering properties as a function of temperature, [MPa]
$\mathbf{M}_{\text{junction}}^M$	Mechanical moment vector at the intersection, [Nmm/mm]
$\mathbf{M}_{\text{junction}}^T$	Thermal moment vector at the intersection, [Nmm/mm]
N	Total number of plies at the intersection, [-]
$\mathbf{N}_{\text{junction}}^M$	Mechanical forces vector at the intersection, [N/mm]
$\mathbf{N}_{\text{junction}}^T$	Thermal forces vector at the intersection, [N/mm]
$\mathbf{N}_{\text{sphere}}^M$	Mechanical forces vector at the sphere, [N/mm]
$\mathbf{N}_{\text{sphere}}^T$	Thermal forces vector at the sphere, [N/mm]
P	Internal pressure, [bar]
P_{FPF}	Internal pressure at which first ply failure occurs, [bar]
P_{LPF}	Internal pressure at which last ply failure occurs, [bar]
P_{MEOP}	Maximum expected operating pressure, [bar]
R	Shell radius, [mm]
R_{fillet}	Intersection fillet radius, [mm]
t	Spherical shell thickness, [mm] Time, [s]
T	Temperature, [°C]
T_o	Initial temperature, [°C]
$\mathbf{T}_{[\varphi]_k}$	Transformation matrix of k ply, [-]
t_{junction}	Junction thickness, [mm]
t_{liner}	Liner thickness, [mm]
t_{ply}	Cured ply thickness, [mm]
V	Internal Volume, [l]
z	Laminate thickness coordinate, [mm]
z_k	Distance of a ply from the laminate mid-plane, [mm]
$\alpha_{11}^T, \alpha_{22}^T$	Ply coefficient of thermal expansion in the direction parallel and transverse to the fibers, 10^{-6} [mm/mm °C]
ε_φ, ε_θ, $\gamma_{\varphi\theta}$	Strain in meridional (φ), hoop (θ) and in-plane shear (φθ) directions, [-]
$\boldsymbol{\varepsilon}_{\varphi,\theta\_\text{junction}}^{[k]}(T,P)$	Strain vector at the intersection of ply k in the laminate coordinate system (φ,θ,φθ) due to P and ΔT, [-]
$\boldsymbol{\varepsilon}_{1,2\_\text{junction}}^{[k]}(T,P)$	Strain vector at the intersection of ply k in the material axis system due to P and ΔT, [-]
$\boldsymbol{\varepsilon}_{\varphi,\theta\_\text{sphere}}^{[k]}(T,P)$	Strain vector at the sphere of ply k in the laminate coordinate system (φ,θ,φθ) due to P and ΔT, [-]

$\boldsymbol{\varepsilon}^{[k]}_{1,2\_sphere}(T,P)$ Strain vector at the sphere of ply k in the material axis system due to P and ΔT, [-]
$\boldsymbol{\varepsilon}^{o}_{sphere}$ Mid-surface strains vector, [-]
$\boldsymbol{\kappa}^{o}_{sphere}$ Mid-surface curvatures vector, [-]
$\boldsymbol{\sigma}^{[k]}_{1,2\_junction}(T,P)$ Stress vector at the intersection of ply k in the material axis system due to P and ΔT, [MPa]
$\boldsymbol{\sigma}^{[k]}_{1,2\_sphere}(T,P)$ Stress vector at the sphere of ply k in the material axis system due to P and ΔT, [MPa]

LH_2 tanks are expected to: i) store hydrogen in large quantities, ii) conform efficiently to a given space within the aircraft, iii) operate at cryogenic conditions and to iv) minimize LH_2 boil-off due to reduced surface area. Cylindrical pressure vessels have been utilized as LH_2 fuel tanks in several published works [4–6]. However it was shown in the Cryoplane Project [7] that cylindrical pressure vessels are not always suitable configurations for fuel containment within an aircraft as they lead to a lot of unused volume. The multi-cell concept has proved to be volumetrically more efficient than packed cylinders when fitted in a prescribed rectangular envelope [8]. It was shown within the same work, that the volumetric efficiency of a multi-cell consisting of intersecting cylinders has an asymptotically increasing trend with an increasing envelope aspect ratio (length/width). A slightly improved configuration can be found in the multi-lobe geometry with intersecting conical cells utilized in the LH_2 tank of X33 vehicle [9]. However in places where the aspect ratio of the enclosing box is closer to 1, the most volumetrically efficient solution is the multi-sphere. A multi-spherical configuration leads to weight savings associated with the more homogeneous shell stresses. Additionally, spheres consist of the minimum surface area for a given volume, and thus minimize heat loss and, consequently, fuel boil-off.

Composite materials have shown excellent potential for lightweight pressure vessel design, because of their tailorability, high strength and high stiffness-to-weight ratios [10,11]. The conceptual use of a composite overwrap at intersecting spheres was presented by Elliot et al. [12], but the manufacturability of such a configuration has always been an issue.

Tapeinos et al. [13] developed a novel composite overwrapped multi-spherical tank configuration with a polymeric liner. The tank consisted of four partially merged spheres, with uni-directional (UD) carbon fiber straps placed at the merging points to introduce strain compatibility between the spheres and intersections. A thorough understanding of the tank behavior under hydrostatic pressure testing and evaluation of the pressure window would be considered beneficial. Additionally, an experimental assessment of the thermal and structural response of the multi-sphere when subjected to nominal cryogenic operation would be a valuable asset.

Hydrostatic pressure testing of composite overwrapped pressure vessels (COPVs) at ambient conditions has been reported in several studies [14–16]. Revilock et al. [17] conducted a hydrostatic burst at a spherical COPV used in Space Shuttle Orbiter to describe its complex mechanical response and establish its pressure allowable. Three dimensional (3D) Digital-Image-Correlation (DIC) was incorporated to evaluate the in-plane full principal strain field over the tank contour that showed that the ultimate structural failure was initiated from liner fracture at the welding line. Acoustic emissions (AE) have been used to assess damage onset and progression as well as classification of damage mechanisms throughout loading of a COPV [18–20]. Choul et al. [21] analyzed the initiation and accumulation of damage events by monitoring the accumulated damage hits at the COPV with increasing pressure values. Blassiau et al. [22] showed that progressive failure of COPVs is controlled by matrix relaxation during pressure increase that leads to an overload of the intact fibers and fiber break clustering.

For the case of cryogenic tanks, there have been several published works on the topic of filling and pressure cycling of COPVs to demonstrate safe operation [23–25]. Kang et al. [26] performed an experimental study that revealed a correlation between the temperature gradient and the cool down pattern for different locations at the tank. Lei et al. [27] analyzed the effect of active pressurization at the tank thermal response. Evaluation of the tank structural behaviour when exposed to this environment is of significant importance. Strain monitoring through the use of Fiber bragg Gratings (FBGs) has been employed in several published works [28–30]. Mizutani et al. [31] performed a real-time strain measurement of a composite LH_2 tank with FBGs (Ormocer coated FBG) sensors during rocket operations. However the establishment of a relationship between strain and temperature at the composite overwrap based on obtained experimental results has been ignored.

Despite the fact that many efforts have focused on the study of progressive failure of composite overwrapped pressure vessels, the evaluation of strain evolution with increasing pressure values as well as the pressure window of composite overwrapped multi-spheres has not addressed yet. Additionally, the effect of cryogenic chill-down and pressure cycling at the thermal and structural response of the multi-sphere has not been assessed experimentally yet.

In this work, the experimental verification of the predictions in [32] is performed. More specifically, the thermo-mechanical performance of the innovative type IV multi-spherical tank of [13] is extensively assessed through hydrostatic burst testing at ambient conditions and pressure cycling at cryogenic conditions. Strain measurements are obtained by DIC and FBGs at room and cryogenic conditions respectively. Additionally, the AE technique is hereby utilized for damage monitoring during pressurization. It is shown throughout the hydrostatic pressure test that damage is avoided at the sphere connecting areas (junctions) by introducing a minimum required number of hoop rings (as derived in [32]). By utilizing the AE technique it is shown that first damage onset and global failure occurs close to the hollow center tube at the composite overwrap in a leak-before-burst sequence (which verifies the FE findings of [32]). Additionally, the temperature

profile and corresponding heat transfer mechanisms over the multi-bubble tank contour due cryogenic chill-down and pressure cycling are evaluated using thermocouples. Furthermore, a relationship between strain and temperature is established. The findings verified the results of the FE results and the approximation functions for coefficient of thermal expansion (CTE) and engineering properties of the composite overwrap derived in [32].

Tank specifications

The geometrical specifications of the sub-scale multi-sphere tank are outlined in Table 1. Four intersecting spheres were employed with a sphere radius $R = 145$ [mm]. As mentioned in [32], Carbon Fiber-Reinforced Polymer (CFRP) patches were draped onto the roto-moulded PA12 liner. The minimum required number of UD straps at [0°] and [±45°] orientations at the intersections was evaluated by using the method presented in [32], on the basis of having a slightly higher stiffness at the intersection in meridional and hoop directions. This will lead the damage onset and ultimate failure at the spheres when loaded under internal pressure or thermo-mechanical loading.

The focus of this study is to perform an experimental assessment of this sub-scale configuration to understand its performance throughout operational loads and compare the experimental results with the findings of the FE analysis in [32]. The various steps followed throughout tank testing and corresponding tank testing guidelines are presented in the next section.

Tank testing

Hydrostatic burst at room temperature

Test description

The test campaign of the sub-scale multi-sphere (presented in Section Tank Specifications) was conducted according to the proof testing requirements of the ANSI/AIAA S-081 standard [33] for composite overwrapped vessels used in reusable launch vehicles (RLVs) and in accordance to the load regime of the LH_2 tank of the SpaceLiner RLV [34]. It is stated in the standard that no burst should occur for internal pressure less than 1.5 times the MEOP, which for the case of the SpaceLiner is 3.8 [bar], resulting in a proof pressure value of 5.7 [bar]. The hydrostatic burst test is used to analyse the tank behaviour when pressurized at a high displacement rate, locate the damage mechanisms and evaluate the pressure allowables. This will give insight on how the tank will behave during a sudden pressure increase in operation e.g. from excessive fuel boil-off, or even from a pressure relieve device malfunction.

Instrumentation

Data acquisition systems that assist in the evaluation of the tank performance during the hydrostatic pressure test and isolation of the locations and load values of damage onset (as well the global structural failure patterns) were used.

Three-dimensional (3D) DIC was employed to record the full in-plane strain field at one side of the tank (Fig. 1b). The DIC system utilized Vic3D software from Correlated Solutions. Spraying high contrast dot patterns (speckles) on the tank surface was required in order to signify all the different strain measurement points. Vic3D tracks the displacement at each dot at each successive pair of images. To calibrate for this volume, the camera resolution was set to 2048 x 2048 [pixels]. Strain measurements at the composite overwrap over time were monitored to quantify the pressure values at which contact would be achieved between the polymeric liner and composite overwrap at different locations (since there was a gap formed between these two bodies throughout the curing stage).

The AE technique was utilized to reveal damage onset and progression as well as its relative corresponding location and thus help to evaluate the multi-spherical COPV pressure allowable. Based on this technique, the tank pressure window -the pressure difference from the very first damage event (P_{FPF}) to final failure (P_{LPF}) - can be evaluated. The AE parameter that was recorded throughout the experiments was the cumulative absolute acoustic energy measure of all the AE hits. Any abnormal change at the acoustic energy response indicates the presence of new damage within the structure. Acoustic energy is evaluated as a function of internal pressure (P).

All the different locations where AE sensors were mounted on the tank surface are shown in Fig. 1a. Sensors #1 and #5 were placed at the bottom spheres and close the central hollow tube. On the other hand, sensors #3 and #4 at the upper spheres were utilized to monitor any unwanted damage onset or even unexpected water leak next to the polar openings. Finally, sensor #2 was mounted next to the horizontal intersection to capture any damage phenomena occurring at the junction or adjacent spherical cells during pressurization.

The complete experimental setup of the tank inside a container where it is pressurized with water is depicted in Fig. 1b. The DIC cameras were incorporated with an inclination angle of [15°] from the horizontal axis to have a focus at the upper half of the multi-cell test specimen. A burst pressure test bench (manufactured from SHINEEAST) with an IPC control unit incorporating LabView Software was employed to build up pressure within the tank.

Table 1 – Specifications of the sub-scale multi-sphere tank.

Liner material	Sphere radius (R)	Intersection fillet radius (R_{fillet})	Centroid distance (d)	Sphere lay-up	Intersection thickness	Liner thickness (t_{liner})	Internal Volume (V)
PA12	145 [mm]	29 [mm]	200 [mm]	$[0,45,-45,90]_s$	3.97 [mm]	6.5 [mm]	46.1 [l]

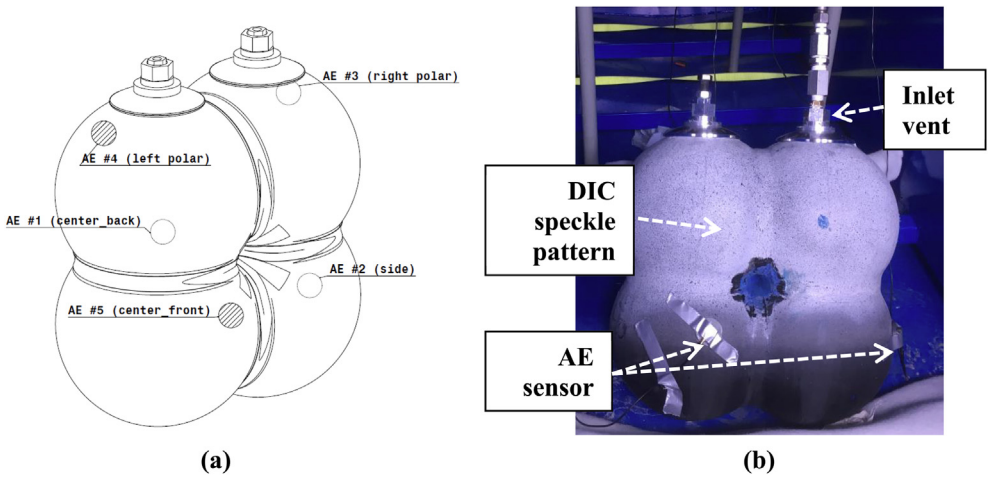

Fig. 1 – a) Layout of the Acoustic Emission (AE) sensors at the tank contour and b) overview of the tank configuration before hydro-burst testing.

Experimental procedure

Water was added through hydraulic pressure hoses to increase the pressure. Real time monitoring of pressure values at a high-sampling speed was performed by using a digital pressure gauge. The tank was pressurized at a $dP/dt = 1.35$ [bar/s] approximately, which corresponds to a fast pressure rise rate that a cryogenic tank is facing throughout cryogen evaporation when lacking a thermal insulation layer [35].

Pressure cycling at cryogenic temperature

Test description

According to ANSI/AIAA S-081 standard [33] the cryogenic tank needs to be subjected to a given number of pressurization cycles at MEOP while storing a cryogenic liquid, where no burst, nor pressure loss may occur throughout the entire cycling procedure. Furthermore, repeated pressure cycling at cryogenic temperatures as well as emptying of the tank represents the multiple filling/draining phases during the structure's lifetime. Throughout pressure cycling at cryogenic temperatures, it is hereby considered critical to assess: i) the temperature profile at the tank contour due to induced chill-down, ii) the dominant heat transfer mechanisms at various tank locations and iii) the effect of temperature on the strain behaviour of the composite overwrap.

Instrumentation

FBGs with an Ormocer coating were applied at the overwrap surface to evaluate strain at different locations throughout the different testing stages (cryogenic chill-down, pressure cycling, draining). The FBG sensors used in this study were LBL-1550-125 draw tower grating (DTG) type sensors (FBGS International NV). The length of the sensors was 8 [mm] with nominal Bragg wavelengths distributed in the range of 1520–1570 [nm]. The PXIe-4844 optical sensor interrogator (from National Instruments) was used to record the FBG outputs where both strain and pressure recording were conducted at 10 [Hz]. Additionally, thermocouples (type K) were glued adjacent to every FBG sensor, in order to obtain a temperature-strain relationship.

The different points on the tank surface where FBGs and thermocouples were mounted can be seen in Fig. 2. The FBGs were divided into 4 groups based on the different regions of interest: i) spherical cells, ii) top intersection and hollow tube, iii) horizontal intersection and hollow tube and iv) polar openings. The focus and local direction of strain measurement of every fiber group is outlined in Table 2. Every FBG group was assigned to assess the temperature and strain gradient along a corresponding path at the tank. The gradient can be either explained because of the location relative to the liquid interface level or the liner and composite overwrap being in contact (or not), which affects the mode of heat transfer and thus the strain behaviour.

The tank surface-mounted FBGs and thermocouples can be seen in Fig. 3a in accordance with the locations shown in Fig. 2. Temperature recordings were performed in another 3 points (at three different heights along the tank lower sphere). Furthermore, a pressure gauge was connected to the pipeline, monitoring the pressure value. For tank pressurisation, an

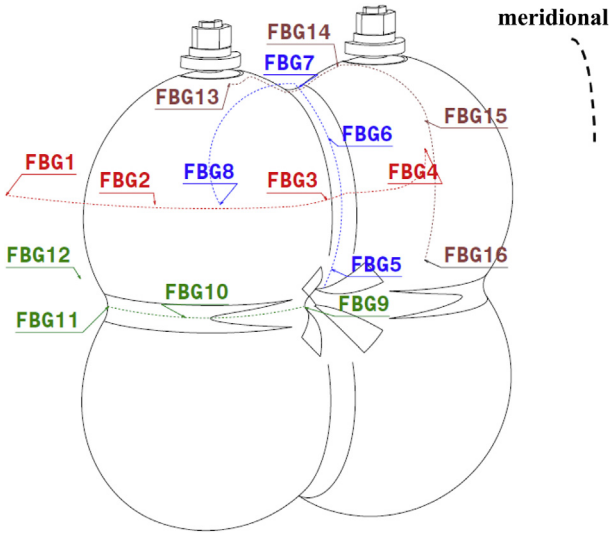

Fig. 2 – Layout of the various FBGs at the tank contour.

Table 2 – Outline of FBGs sensors.

	1	2	3	4	5	6	7	8	9	10	11	12	13	14	15	16
Direction	H	H	H	M	M	M	M	M	M	M	M	M	H	H	H	H
Group	Spheres				Top Intersection & Center				Horizontal Intersection & Center				Openings & Sphere			
Focus	T, ε distribution from sphere to the intersection at liquid interface level				T, ε distribution along the intersection above and below liquid interface level				T, ε distribution along the horizontal intersection and the center				T, ε distribution next to openings at vapour region			

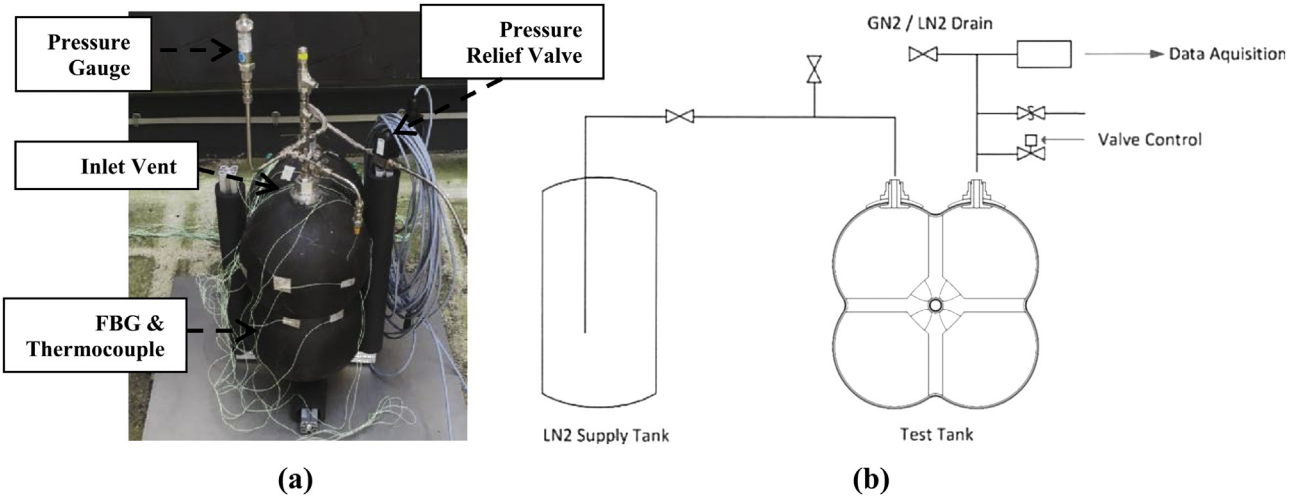

Fig. 3 – a) Overview of the experimental setup and sensors before testing and b) complete lay-out of all systems of the test setup.

inlet vent was used to insert gaseous nitrogen (GN_2) while another outlet vent was utilized to drain the system. The complete lay-out of the test setup can be seen in Fig. 3b.

Experimental procedure

For this experiment, LN_2 was used instead of LH_2 for safety reasons. The boiling point of LN_2 is −196 [°C], which is slightly higher than LH_2 (−253 [°C]). All loading stages that the SpaceLiner liquid hydrogen (LH_2) tank was subjected to -during operation-were taken into consideration [34]. These include i) nominal cryogenic operation at MEOP (at 3.8 [bar]), ii) nominal empty operation after main engine cut-off (MECO) at MEOP (at 3 [bar]) and iii) off-nominal operation after early MECO with remaining fuel (at 3.5 [bar]). The test procedure consisted of the following steps:

1. Filling of the test tank with LN_2 to a level of 75 [%] by volume (filling rate: 0.0055 [l/s]).
2. Stepwise active pressurization (with the use of GN_2 at 20 [°C]) to 3 [bar], 3.5 [bar] and 3.8 [bar].
3. Unloading to atmospheric pressure.
4. Repetition of steps 2–3 by five times (simulation of filling/draining).
5. Draining of the tank (low vacuum: 50 [mbar]).

Throughout the chill-down process ambient air was cooled below its dew point through contact with the colder tank wall surface. This led to water vapour condensation; since the temperature was below water freezing point, frost was formed all over the tank surface. Complete de-icing occurred only after some time following the draining phase.

Results

Hydrostatic burst at room temperature

The internal pressure levels as a function of time can be seen in Fig. 4. The following events occurring at different pressure values are illustrated:

i) liner-to-overwrap gradual contact (3.7 [bar] $\leq P \leq$ 8.4 [bar]),
ii) liner and overwrap damage onset and evolution (7.2 [bar] $\leq P \leq$ 18.84 [bar]),
iii) burst at $P =$ 18.84 [bar].

The liner deformation could not be monitored throughout the test, so the focus was given on the composite overwrap.

It was shown in [32] that contact between the liner and composite overwrap was progressively taking place with increasing pressure, where the central tube was the first contact region. This is verified in Fig. 5, where strain jumps at the overwrap were triggered by liner-overwrap contact and thus load transfer occurs from one layer to the other. The meridional strain distribution from the sphere center to the

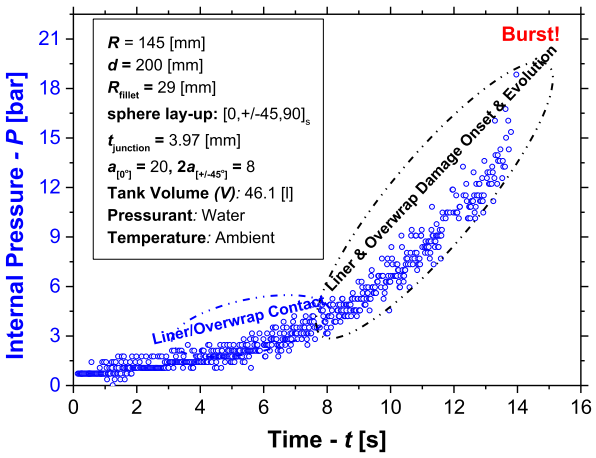

Fig. 4: Internal pressure vs time.

Fig. 4 – Internal pressure vs time.

intersection tip (half-way through the arc length of an intersection) is shown at various *P* values. Meridional direction can be seen in Fig. 2. These values correspond to contact being achieved at a) the bottom, b) top and c) middle sections of the intersection/sphere boundary regions. The small multi-sphere figures depict the corresponding locations at the tank. Fig. 5d shows the strain distribution at all locations, right before burst occurs.

Due to the fact that strain accumulated at a faster rate at the sphere/intersection boundary (because of contact), first damage onset and complete loss of load carrying capability was expected to occur in those regions. Fig. 6a depicts the cumulative acoustic energy combined for all sensors as a function of internal pressure. As expected, a highly non-linear behaviour was obtained, having a sudden increase at 7.2 [bar] approximately (signifying damage initiation) while reaching a peak value at 18.84 [bar] (attributed to global failure). This first damage onset can be seen in Fig. 6b, where the acoustic energy in AE sensors #1,2,3,5 became larger than zero. The initial low energy levels in AE sensor #4 can be associated to liner/composite overwrap contact. It is evident that the largest absolute energy levels were recorded in AE sensor #5 (Fig. 1) right before failure, signifying excessive damage accumulation next to the central tube leading to pressure loss at 18.84 [bar], as expected in [32].

A comparison of the FE analysis and the hydrostatic burst pressure test results on locations and global failure mechanisms can be seen in Fig. 7a and b respectively. Loss of load carrying capability occurred in both cases close to the central hollow cylindrical tube and at the spherical cells, signifying the same global failure location. Failure can be attributed to through-the-thickness matrix cracking of the laminate triggered by liner fracture. The burst pressure value was 23.35 [bar] in the FE analysis while in the experiment it was 18.84 [bar] (offset of 23 [%]). Furthermore, a water leak occurred at

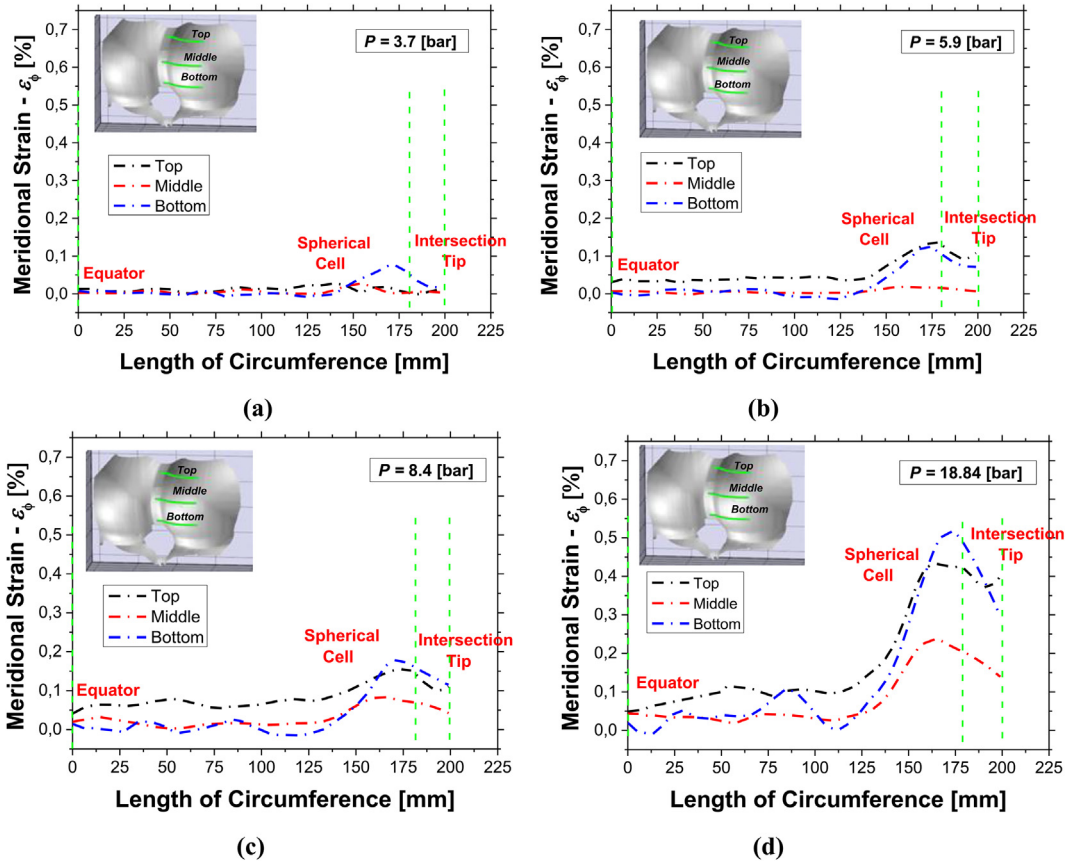

Fig. 5 – Meridional strain distribution over the spherical shells and top, middle and bottom part of the junction for distinctive pressures values (P) with contact liner/overwrap.

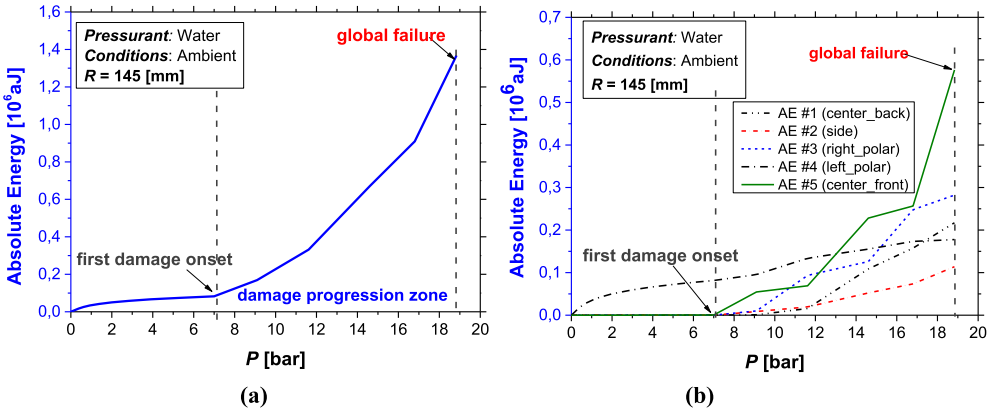

Fig. 6 – a) Cumulative absolute acoustic energy of all AE sensors combined and b) cumulative absolute acoustic energy per AE sensor as a function of increasing internal pressure.

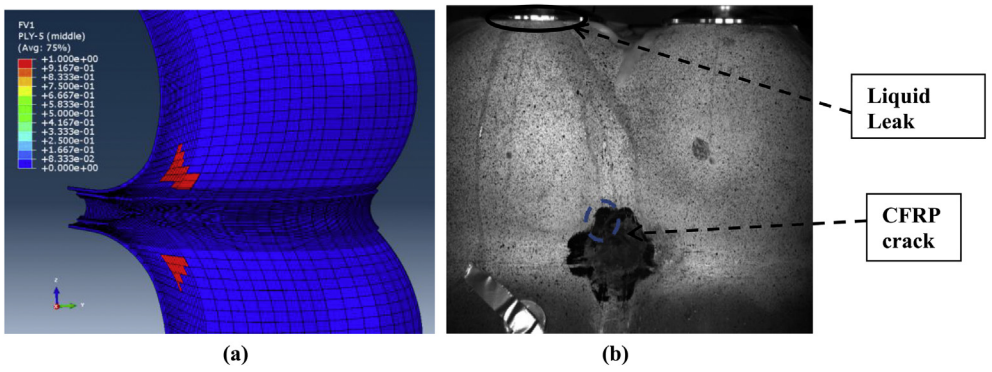

Fig. 7 – Ultimate structural failure pattern (pressure loss) for the tank (cracked liner & matrix cracks through-the-thickness) a) at 23.35 [bar] from FE analysis [32] and b) at 18.84 [bar] from the burst test.

one metallic boss connection at the depicted polar opening of Fig. 7b, at the time of overwrap failure next to the central hollow tube. Despite a crack in the liner at the vicinity of the boss, DIC measurements and AE readings did not indicate any damage at the corresponding region at the composite overwrap.

A comparison between the FE [32] and AE results regarding the damage evolution and pressure loss (cluster of matrix cracks under tension) is shown in Fig. 8. The multi-spherical COPV underwent first-ply failure (FPF) at 7.2 [bar] at the test (SF = 1.89 times the MEOP) as opposed to 9.2 [bar] for the FE analysis (SF = 2.42 times the MEOP); this leads to an offset of 16.3 [%] in the tank pressure window dP value (P_{LPF}- P_{FPF}) between the experiment and FE analysis.

Additionally, a comparison of the tank pressure window when loaded at high (dP/dt = 1.35 [bar/s]) and low (dP/dt = 0.05 [bar/s]) pressure rise rate is depicted in Fig. 8, based on the FE model findings of [32] and experimental results. The pressure window for the low pressure rise rate case was dP_slow_FE = 42.6 [bar], while for the high pressure rise rate case it was dP_fast_FE = 14.1 [bar] for the FE analysis and dP_fast_exp = 11.8 [bar] for the experiment. The difference in the pressure window between the two high and low pressure rise cases lies on the fact that the liner elongates freely without any damage onset when loaded at a low pressure rise rate and the pressure load is transferred to the overwrap. Subsequently, the strength of the fibers is fully utilized and thus the global failure mechanism is fiber breakage whereas for the high pressure rise rate liner fracture and matrix cracking results in pressure loss.

It was shown, that by introducing a minimum required number of UD straps (based on method provided in [32]), damage is avoided at the intersections (being a region that is

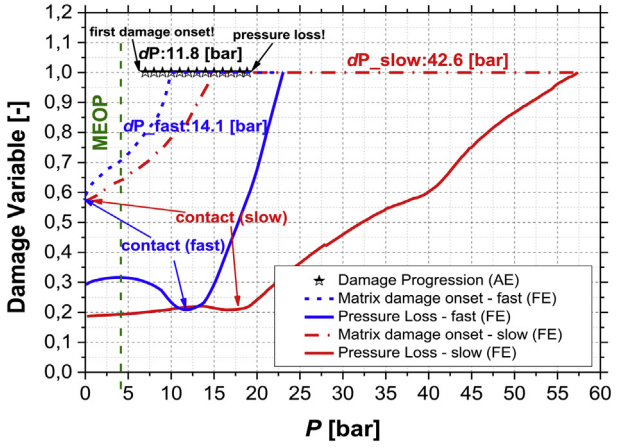

Fig. 8 – Tank pressure window based on experiment and FE analysis.

difficult to inspect). Finally, damage onset and evolution obtained a very localized behavior (at the sphere and next to the central tube) owing to faster strain accumulation linked to liner/overwrap contact at that region. In the next section the results of the cryogenic test are outlined.

Pressure cycling with LN_2

Both the temperature at the upper sphere (FBG #16) and internal pressure as a function of time during the cryo test can be seen in Fig. 9. The stages of the test were:

i) cryogenic chill-down due to filling of tank with LN_2 (0 [s] $\leq t \leq$ 6000 [s]),
ii) steady state condition (6000 [s] $< t \leq$ 10000 [s]),
iii) pressure cycling (10000 [s] $< t \leq$ 12000 [s]) and
iv) tank draining (12000 [s] $< t \leq$ 14000 [s]).

The temperature on the entire tank wall was dictated by any of the following four ways of heat transfer:

i) natural convection (at the vapour region),
ii) radial thermal conduction at the vessel walls,
iii) circumferential thermal conduction at the vessel walls,
iv) convection associated with LN_2 boiling (at the liquid interface level).

Throughout this test, the liner performance could not be monitored so the focus was given on the composite overwrap. According to FBG #16 (location can be seen in Fig. 2), the first three heat transfer modes were the primary mechanisms of wall cooling that took place until 5500 [s] approximately (Fig. 9). From the moment that the LN_2 level passed sensor #16 a very sudden temperature decrease was recorded from 5500 [s] to 6000 [s] due to liquid boiling. The composite overwrap in this location did not reach LN_2 saturation temperature (−196 [°C]) due to the air gap formed between itself and the liner. At the end of the chill-down stage ($t = 5500$ [s]), cracking occurred at the liner (central cylindrical tube) that led to continuous infiltration of LN_2 the composite overwrap. Addition of pressurant (GN_2 at room temperature) led to rapid LN_2 evaporation, which was reflected by the temperature increase in Fig. 9. Finally, sensor #16 indicated linearly increasing temperature

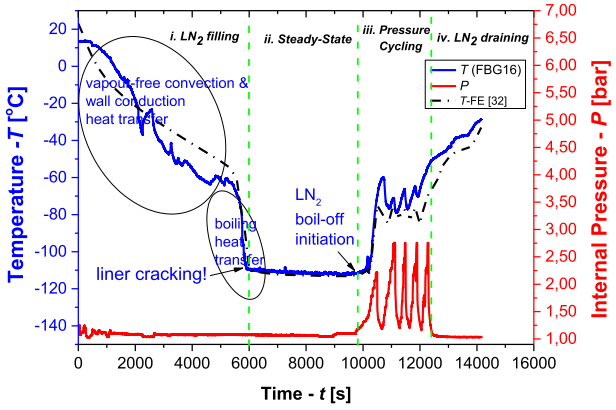

Fig. 9 – Temperature and internal pressure history at the upper sphere (FBG #16) versus time.

over time at the draining stage. A comparison between the FE analysis of [32] and the experiment revealed a close agreement in the temperature evolution. A temperature offset (12 [°C] approximately) at the beginning of the pressure cycling can be explained by the GN_2 infiltration through the cracked liner that led to a small temperature increase at the overwrap.

The temperature history for various locations at the composite overwrap can be seen in Fig. 10. The results from FBGs #2,3,4,8,11,13 (Fig. 2) are not plotted since they are symmetrically placed to FBGs #1,5,10,14. It is evident that the higher the prescribed sensor position, the more time it stays in the vapour region where it is cooling down at a slower rate due to natural convection and circumferential conduction being the two main heat transfer mechanisms. With the liquid level increasing, temperature values at all measurement points were dropping while most of them obtained a temperature plateau when the tank was filled up to 75 [%] of its volume.

A temperature plateau was reached after the chill-down stage at the ullage region (FBGs #6,7,14) where the effect of pressure cycling did not lead to temperature fluctuations. On the other hand, the points that were close to the gas/liquid interface level (FBGs #1,15) did not reach a temperature plateau due to LN_2 boil-off that led to small localised temperature increase. A plateau was also obtained at the mid-tank level (FBGs #5,9,10,12,16), but a large sudden temperature increase (50 [°C] approximately in a span of 1000 [s]) was recorded due to the introduction of warm pressurant gas (GN_2) that resulted in LN_2 vaporization. Lower temperatures were recorded at the bottom spheres (FBGs # 17,18,19) that can be linked to the fact that the tank was filled up to 75 [%] and the thicker frost layer (due to more accumulated water vapour condensation over time). The frost layer that was developed at the outer surface of the overwrap behaved like a thermal insulator that eliminated passive heat from the exterior.

For the tank deformation during cryo-cycling, the corresponding strain values at the spheres and intersections are depicted in Fig. 11a and b respectively. The sensor locations can be seen in Fig. 2. It can be seen that the cryogenic environment led to contraction of the tank wall and thus the trend of compressive strain was directly influenced by the temperature profile at every sensor (Fig. 10). Recorded strain values in all intersection locations were lower in amplitude than the strain measured at the undisturbed spherical areas (Fig. 11b). This is attributed to the fact that the CTE of the laminate is considerably lower in the intersections (because of all the added [0°] plies) than at the spheres. Additionally, the effect of pressure cycling stage was more evident in the intersections at FBGs #8 and #9, because the overwrap was in contact with the liner at those locations and load transfer occurred. The recorded strain values were significantly lower than the strain allowables of [32] and could not result in any damage onset in the composite overwrap. Visual inspection of the composite overwrap showed no signs of damage.

At this point, it is crucial to evaluate strain as a function of temperature and pressure at the overwrap based on a basic thermo-elastic load-deformation relationship (from Classical Lamination Theory-CLT [36]) and compare this to the findings to experimental recordings. The comparison will allow for verification of the approximation functions derived in [32]. Strain as a function of temperature (T) and pressure (P) for any

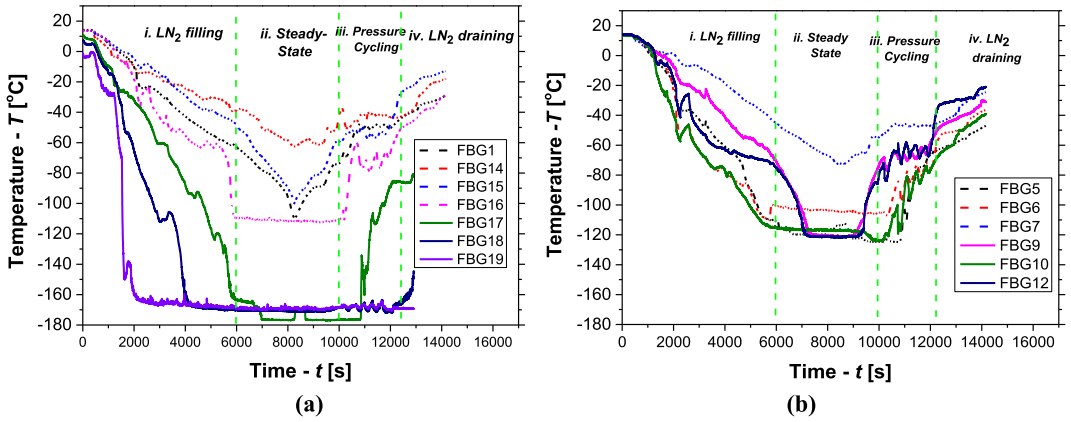

Fig. 10 – Temperature history over the a) spheres and b) intersections throughout i) LN_2 filling, ii) steady-state, iii) pressure-cycling and iv) draining stages.

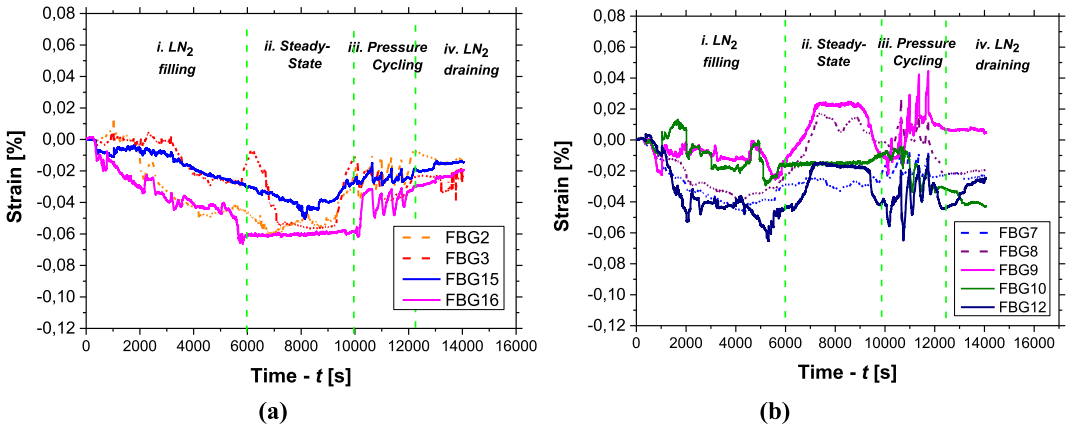

Fig. 11 – Strain distribution over the a) spheres and b) intersections throughout i) LN_2 filling, ii) steady-state, iii) pressure-cycling and iv) draining stages.

ply k of the quasi-isotropic laminate (QI) in the material axis system is given by [36]:

$$\boldsymbol{\varepsilon}^{[k]}_{1,2\_sphere}(T,P) = \mathbf{T}_{[\varphi]_k} \cdot \boldsymbol{\varepsilon}^{[k]}_{\varphi,\theta\_sphere}(T,P), \tag{1}$$

where

$$\begin{aligned}\boldsymbol{\varepsilon}^{[k]}_{\varphi,\theta\_sphere}(T,P) &= \boldsymbol{\varepsilon}^{o}_{sphere} + z\boldsymbol{\kappa}^{o}_{sphere} - \mathbf{e}^{[\varphi_k]}_{free} \\ &= \left(\mathbf{A}_{sphere}(T)\right)^{-1} \cdot \left[\mathbf{N}^{M}_{sphere} + \mathbf{N}^{T}_{sphere}\right] - \mathbf{e}^{[\varphi_k]}_{free},\end{aligned} \tag{2}$$

$$\begin{aligned}\mathbf{e}^{[0^\circ]}_{free} &= \begin{bmatrix} \alpha^{T}_{11}\Delta T \\ \alpha^{T}_{22}\Delta T \\ 0 \end{bmatrix}, \mathbf{e}^{[\pm 45^\circ]}_{free} \\ &= \begin{bmatrix} \alpha^{T}_{11}\cos(\pm 45)^2 + \alpha^{T}_{22}\sin(\pm 45)^2 \\ \alpha^{T}_{11}\sin(\pm 45)^2 + \alpha^{T}_{11}\sin(\pm 45)^2 \\ 2(\alpha^{T}_{11} - \alpha^{T}_{22})\cos(\pm 45)\sin(\pm 45) \end{bmatrix} \Delta T, \mathbf{e}^{[90^\circ]}_{free} = \begin{bmatrix} \alpha^{T}_{22}\Delta T \\ \alpha^{T}_{11}\Delta T \\ 0 \end{bmatrix},\end{aligned} \tag{3}$$

$$\mathbf{N}^{T}_{sphere} = 2t_{ply}\left(\mathbf{C}_{[0^\circ]}(T) \cdot \mathbf{e}^{[0^\circ]}_{free} + \mathbf{C}_{[\pm 45^\circ]}(T)\mathbf{e}^{[\pm 45^\circ]}_{free} + \mathbf{C}_{[90^\circ]}(T) \cdot \mathbf{e}^{[90^\circ]}_{free}\right), \tag{4}$$

$$\mathbf{N}^{M}_{sphere} = \begin{bmatrix} PR/2 \\ PR/2 \\ 0 \end{bmatrix} \tag{5}$$

and $\boldsymbol{\varepsilon}^{[k]}_{\varphi,\theta\_sphere}(T,P)$ is the strain vector in the laminate coordinate system $(\varphi,\theta,\varphi\theta)$ and $\boldsymbol{\kappa}^{o}_{sphere}$ are the mid-plane strains and curvatures respectively, $\mathbf{e}^{[\varphi_k]}_{free}$ is the free expansion strain vector of layer k and z is the laminate thickness coordinate. Curvatures $(\boldsymbol{\kappa}^{o}_{sphere})$ due to ΔT are zero at the sphere, owing to the balanced and symmetric QI lay-up. The symbols $\mathbf{N}^{T}_{sphere}$ and $\mathbf{N}^{M}_{sphere}$ correspond to the thermal and mechanical forces vectors respectively. The parameter $(\mathbf{A}_{sphere}(T))^{-1}$ represents the QI laminate extensional compliance matrix as a function of temperature. The temperature drop (ΔT) is assumed as uniform through the thin-walled overwrap.

Strain at the intersections can be calculated by employing Eqs. 6–10 [36].

$$\boldsymbol{\varepsilon}^{[k]}_{1,2\_junction}(T,P) = \mathbf{T}_{[\varphi]_k} \cdot \boldsymbol{\varepsilon}^{[k]}_{\varphi,\theta\_junction}(T,P) \tag{6}$$

$$\varepsilon^{[k]}_{\varphi,\theta\_junction}(T,P) = (\mathbf{A}_{torus}(T))^{-1}\cdot\left[\mathbf{N}^{M}_{junction} + \mathbf{N}^{T}_{junction}\right] + z(\mathbf{D}_{torus}(T))^{-1}\cdot\left[\mathbf{M}^{M}_{junction} + \mathbf{M}^{T}_{junction}\right] - \mathbf{e}^{[\varphi_k]}_{free}, \quad (7)$$

where

$$\mathbf{N}^{T}_{junction} = t_{ply}\left(a_{[0^\circ]}\mathbf{C}_{[0^\circ]}(T)\cdot\mathbf{e}^{[0^\circ]}_{free} + a_{[\pm45^\circ]}\mathbf{C}_{[\pm45^\circ]}(T)\cdot\mathbf{e}^{[\pm45^\circ]}_{free}\right), \quad (8)$$

$$\mathbf{M}^{T}_{junction} = z_k t_{ply}\left(a_{[0^\circ]}\mathbf{C}_{[0^\circ]}(T)\cdot\mathbf{e}^{[0^\circ]}_{free} + a_{[\pm45^\circ]}\mathbf{C}_{[\pm45^\circ]}(T)\cdot\mathbf{e}^{[\pm45^\circ]}_{free}\right), \quad (9)$$

$$\mathbf{D}_{torus}(T) = \frac{1}{3}\sum_{\kappa=1}^{N}\left(\mathbf{C}_{[\varphi]_k}(T)\right)\left(z_k^3 - z_{k-1}^3\right), N = a_{[0^\circ]} + 2a_{[\pm45^\circ]} \quad (10)$$

And $(\mathbf{D}_{torus}(T))^{-1}$ is the bending laminate compliance matrix of the toroidal shell as a function of temperature, z_k is the distance of a ply from the laminate mid-plane and N is the number of plies at the intersection and as mentioned in [32] the laminate at the toroidal shell consists of [0°] and [±45°] plies, which number is given by $a_{[0^\circ]}$ and $2a_{[\pm45^\circ]}$ respectively. The symbols $\mathbf{N}^{T}_{junction}$ and $\mathbf{N}^{M}_{junction}$ correspond to the thermal and mechanical forces vectors respectively, while $\mathbf{M}^{T}_{junction}$ and $\mathbf{M}^{M}_{junction}$ are the thermal and mechanical moments vectors respectively at the sphere/intersection junction and are derived in [32]. The engineering constants E^{T}_{11}, E^{T}_{22} and G^{T}_{12} as well as the CTE of the composite ply at the longitudinal (a^{T}_{11}) and transverse (a^{T}_{22}) directions were derived in [32] using Eqs 11 and 12:

$$(E^{T}_{11}, E^{T}_{22}, G^{T}_{12}) = f(a,b,c|T) \Rightarrow \frac{a}{1+be^{-cT}} \quad (11)$$

$$(\alpha^{T}_{11}, \alpha^{T}_{22}) = f(a,b,c,a^{\circ}|T) \Rightarrow aT^3 + bT^2 + cT + \alpha^{\circ} \quad (12)$$

Strain as a function of temperature is illustrated in Fig. 12 at the sphere at two different locations: at the vapour region (FBG #15) and below the liquid level (FBG #16). The exact location of the sensors and corresponding direction of strain measurement (hoop) can be seen in Fig. 2. A comparison between the results of CLT, the FE analysis and experimental recordings is hereby shown.

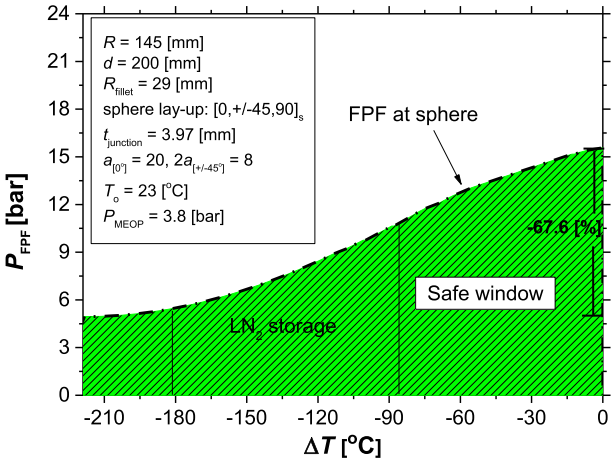

Fig. 13 – Pressure allowable as a function of inner temperature for the overwrap based on Hashin criterion.

Higher compressive strain values can be seen below the liquid level, which is caused by the larger ΔT that the overwrap is subjected to. As expected, a non-linear relationship between hoop strain and temperature can be seen in both Fig. 12a and b. It is shown in Fig. 12b that the temperature effect on strain sensor #16 was not so strong below −70 [°C] approximately, owing to a closer compaction of the material molecules and increase of its stiffness at lower cryogenic temperatures. The FE and experimental values of strain showed good agreement (average offset of 9.5 [%]) with a small offset for $-40 \le T \le 10$ [°C] (and a maximum offset of 19 [%] offset for −10 [°C]) for FBGs#15,16. On the other hand, CLT and experimental values had average offset of 8.3 [%]. As a result the accuracy of the approximation functions and FE model developed in [32] is verified.

The pressure allowable of the experimentally assessed multi-sphere as a function of varying ΔT is presented in Fig. 13. The effect of overwrap curing (prior to cryogenic operation) is also taken into consideration. The approach is based on the evaluation of ply stresses at the principal material axes system at the spheres (Eq. (13)) and at the intersections (Eq. (14)) and applying the Hashin failure criterion to check for first-ply

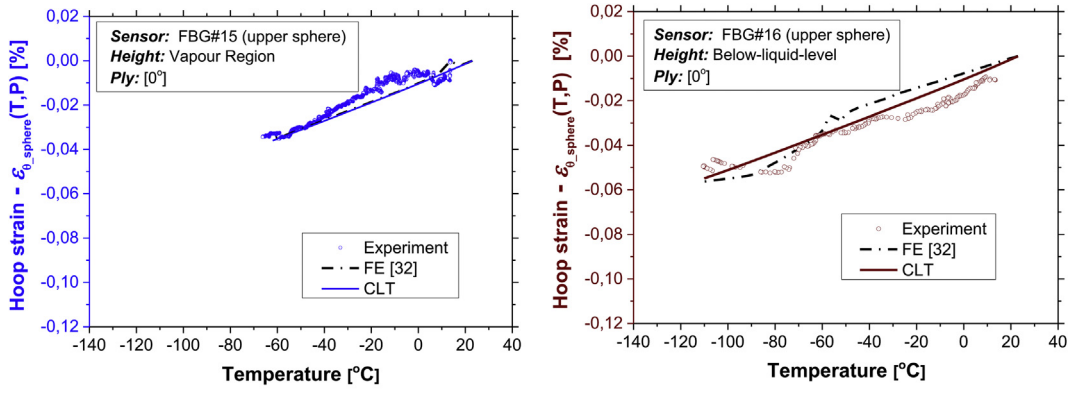

Fig. 12 – Correlation between hoop strain and temperature for the sphere at the a) vapour region and b) below-the-liquid level for the chill-down stage.

failure (FPF) at the fiber or matrix [37]. The ply strength allowables in the parallel and transverse to fiber as well as in-plane shear directions as a function of temperature are identified in [32].

$$\boldsymbol{\sigma}^{[k]}_{1,2\_\text{sphere}}(T,P) = \mathbf{T}_{[\varphi]_k} \cdot \mathbf{C}_{[\varphi]_k}(T) \cdot \boldsymbol{\varepsilon}^{[k]}_{\varphi,\theta\_\text{sphere}}(T,P) \quad (13)$$

$$\boldsymbol{\sigma}^{[k]}_{1,2\_\text{junction}}(T,P) = \mathbf{T}_{[\varphi]_k} \cdot \mathbf{C}_{[\varphi]_k}(T) \cdot \boldsymbol{\varepsilon}^{[k]}_{\varphi,\theta\_\text{junction}}(T,P) \quad (14)$$

The curve depicted in Fig. 13 corresponds to FPF at the transverse direction to the fibers at the sphere. The pressure allowable follows a sigmoid trend (s-curve), owing to the nature of the $E(T)$ and $CTE(T)$ functions in [32].

A reduction of 67.6 [%] in the P_{FPF} value was obtained for $\Delta T = -219$ [°C] compared to the P_{FPF} value at RT ($\Delta T = 0$ [°C]), linked to the overwrap embrittlement at cryogenic temperatures.

Conclusions

In this work, an extensive experimental assessment for the thermomechanical response of a multi-sphere type IV COPV is presented. The multi-spherical COPV incorporates a polymeric liner (Type IV) and four quasi isotropic, merged spherical chambers (scaled to 46.1 [l]). The experimental program consisted of hydrostatic pressure testing at room temperature at a high pressure rise rate as well as cryogenic chill-down and pressure cycling. Strain measurements were obtained by DIC and FBGs at room and cryogenic conditions respectively. Additionally, the AE technique was hereby used to analyze the progressive failure of the multi-sphere during pressurization. The obtained results have been employed for a comprehensive comparison with the analytical and FE-based modelling procedures as outlined in [32].

Throughout the hydrostatic pressure test, it is shown that the introduction of the right number of UD straps leads to damage onset being avoided in the intersections. Damage onset and evolution is characterized by a very localized behavior (at the sphere and next to the central tube) owing to faster strain accumulation linked to liner/overwrap contact at that region. Global failure is triggered by liner rupture and matrix cracking at the spheres near the central hollow cylinder, which verifies the FE findings of [32] with an offset of 23 [%] for the burst pressure value. A comparison between the FE [32] and AE results on the evolution of damage showed a very good agreement (offset of 16.3 [%]) in the tank pressure window (P_{LPF} - P_{FPF}).

For the case of pressure cycling at a cryogenic temperature (with the use of LN_2), the different heat transfer mechanisms at the tank wall were identified. The obtained temperature profile and corresponding strain recordings over the multi-bubble tank surface verified the results of the FE analysis in [32]. A non-linear relationship between strain and temperature was established, where higher compressive strain values were obtained below-the-liquid level due to larger ΔT that the overwrap. Strain recordings at the composite overwrap verified the accuracy of the approximation functions (with an average offset of 9.5 [%]) for $CTE(T)$ and $E(T)$ used in the FE model in [32]. It was shown by using the CLT and approximation functions of [32] that the tank pressure allowable is decreasing in a sigmoid trend (s-curve) with decreasing temperatures. A reduction of 67.6 [%] in the P_{FPF} value is obtained at $T = -196$ [°C] compared to the P_{FPF} value at ambient conditions.

It was however shown that at the end of the cryogenic chill-down stage, liner cracking was formed at the central hollow tube due to difference in CTE values between the composite overwrap and the liner materials (PA12). Damage onset in the liner did not affect the structural integrity of the composite overwrap, and no pressure loss was observed. Liner cracking can be tackled by employing a polymer with lower CTE and higher ultimate failure strain at cryogenic temperatures, whereby the material should be suitable for moulding processes that provide better thickness control.

Future work should focus at the evaluation of different liner materials for a Type IV multi-sphere COPV, to assess whether testing at cryogenic temperatures can be carried out without any damage onset. Additionally, strain monitoring of the multi-sphere throughout the curing process would enable the evaluation of residual stresses from manufacturing.

Acknowledgements

This research has been funded by the 'Cryogenic Hypersonic Advanced Tank Technologies' project (coordinated by DLR-SART) supported by the EU within the 7th Framework Program Theme 7 Transport, Contract no: ACP1-GA-2011-285117. Additionally, it has been supported by the TKI 'Smart Sensing for Aviation' project, sponsored by the Dutch Ministry of Economic Affairs under the Topsectoren policy for High Tech Systems and Materials.

REFERENCES

[1] Brewer GD. Hydrogen aircraft technology. CRC Press; 1991.
[2] Westenberger A. Final Technical Report: liquid hydrogen fuelled aircraft - system analysis. 2003.
[3] Thomas G. Overview of storage development. DOE Hydrogen Program: Annual Review; 2000.
[4] Verstraete D, Hendrick P, Pilidis P, Ramsden K. Hydrogen fuel tanks for subsonic transport aircraft. Int J Hydrogen Energy 2010;35:11085–98.
[5] Verstraete D. Long range transport aircraft using hydrogen fuel. Int J Hydrogen Energy 2013;38:14824–31.
[6] Khandelwal B, Singh R. Hydrogen powered aircraft: the future of air transport. Process in Aerospace Sciences 2013;60:45–59.
[7] Westenberger A. Liquid hydrogen fuelled aircraft – system analysis. Final Technical Report-CryoPlane Project 2003.
[8] Haaland A. High-pressure conformable hydrogen storage for fuel cell vehicles. In: Proceedings of the U.S. DOE Hydrogen Program Review; 2000. California.
[9] Final report of the X-33 liquid hydrogen tank test investigation. Huntsville: NASA Marshall Space Flight Center; 2000.
[10] Schneider J, Dyess M, Hastings C, Patterson J, Noorda J,T. DeLay. Lightweight cryogenic Composite Over-wrapped Pressure Vessels (COPVs) for launch vehicle applications. In: Proceedings of the 48th AIAA Conference; 2007. Hawaii.

[11] Emerson D, Ruby M, Almond D, Turner M, Clarke A. All-thermoplastic composite hydrogen storage cylinders for fuel-cell powered passenger vehicles. In: Proceedings of the 14th automotive composites conference & exhibition (ACCE); 2014. Detroit.
[12] Elliot DR, Francois E, McDonald D. Deep submergence vessels of interconnected radial-filament spheres. USA Patent 1970;3608767.
[13] Tapeinos IG, Koussios S, Groves RM. Design and analysis of a multi-cell subscale tank for liquid hydrogen storage. Int J Hydrogen Energy 2016;41:3676–88.
[14] Tam WH, Griffin PS, Jackson AC. Design and manufacture of a composite overwrapped pressurant tank assembly. In: Proceedings of the 38th. Indiana: AIAA/ASME/SAE/ASEE Joint Propulsion Conference & Exhibit; 2002.
[15] Wang L, Zheng C, Luo H, Wei S, Wei Z. Continuum damage modeling and progressive failure analysis of carbon fiber/epoxy composite pressure vessel. Compos Struct 2015;134:475–82.
[16] Ramirez JPB, Halm D, Grandidier J-C, Villalonga S, Novy F. 700 bar type IV high pressure hydrogen storage vessel burst – simulation and experimental validation. Int J Hydrogen Energy 2015;40:13183–92.
[17] Revilock DM, Thesken JC, Schmidt TE, Forsythe BS. 3D digital image correlation of a composite overwrapped pressure vessel during hydrostatic pressure tests. In: Proceedings of the semi annual conference and exposition on the experimental and applied mechanics. Springfield; 2007.
[18] Mizutani Y, Salga K, Nakamura H, Takizawa N, Arakawa T, Todoroki A. Integrity evaluation of COPVs by means of acoustic emission testing. In: Proceedings of the 2^{8th} european conference on AE testing, Krakow; 2008.
[19] Hill EvK. Predicting burst pressures in filament-wound composite pressure vessels by using acoustic emission data'. Mater Eval 1992;50:1439–45.
[20] Dong L, Mistry J. Acoustic emission monitoring of composite cylinders. Compos Struct 1998;40:43–53.
[21] Chou HY, Mouritz AP, Bannister MK, Bunsell AR. Acoustic emission of composite pressure vessels under constant and cyclic pressure. Composites Part A 2015;70:111–20.
[22] Blassiau S, Bunsell AR, Thionnet A. Micromechanics, damage and life prediction of carbon fibre composite pressure vessels. In: Proceedings of the 11th ECCM, Rhodes; 2004.
[23] Fedorov VI, Luk'yanova EA. Filling and storage of cryogenic propellant components cooled below boiling point in rocket tanks at atmospheric pressure. Chem Petrol Eng 2000;36:584–7.
[24] Kim SY, Kang BH. Thermal design analysis of a liquid hydrogen vessel. Int J Hydrogen Energy 2000;25:133–44.
[25] Messinger RRR. Thermal-mechanical cyclic test of a composite cryogenic tank for reusable launch vehicles. In: Proceedings of the 44th AIAA/ASME/ASCE/AHS/ASC structures. Virginia: Structural Dynamics and Materials Conference; 2003.
[26] Kang Z, Yanzhong L, Yuan M, Lei W, Fushou X, Jiaojiao W. Experimental study on coold down characteristics and thermal stress of cryogenic tank during LN2 filling process. Appl Therm Eng 2018;130:951–61.
[27] Lei W, Yanzhong L, Yonghua J, Yuan M. Experimental investigation on pressurization performance of cryogenic tank during high-temperature helium pressurization process. Cryogenics 2015;66:43–52.
[28] Blazejewski W, Czulak A, Gasior P, Kaleta J, Mecha R. SMART composite high pressure vessels with integrated Optical Fiber Sensors. Proc SPIE 2010:7647.
[29] Güemes A, Frovel M, Pintado JM, Baraibar I, del Olmo E. Fiber optic sensors for hydrogen cryogenic tanks. In: Proceedings of the 2nd european conference on structural health monitoring, munich; 2004.
[30] Latka I, Ecke W, Höfer B, Chojetzki C, Reutlinger A. Fiber optic sensors for the monitoring of cryogenic spacecraft tank structures. In: Proc SPIE5579; 2004. Bellingham-WA.
[31] Mizutani T, Takeda N,H. Takeya on-board strain measurement of a cryogenic composite tank mounted on a reusable rocket using FBG sensors. Struct Health Monit 2006;5:205–14.
[32] Tapeinos I.G., Zarouchas D.S., Bergsma O., Koussios S., Benedictus R., Evaluation of the mechanical performance of a multi-cell tank for cryogenic storage: Part I- tank pressure window based on progressive failure analysis, Int J Hydrogen Energy, (accepted).
[33] Chang JB. Implementation guidelines for ANSI/AIAA S-081: space systems composite overwrapped pressure vessels. 2003.
[34] CHATT Project, 'Final Report', 2015.
[35] Agrawal G, Joseph J, Agarwal DK, Kumar SS. Effect of insulation thickness on evolution of pressure and temperature in a cryogenic tank. In: Proceedings of the 23rd national heat and mass transfer conference, India; 2015.
[36] Daniel IM, Ishai O. Engineering mechanics of composite materials. 2nd ed. Oxford University Press; 2006.
[37] Hashin Z. Failure criteria for unidirectional fiber composites. J Appl Mech 1980;47:329–34.